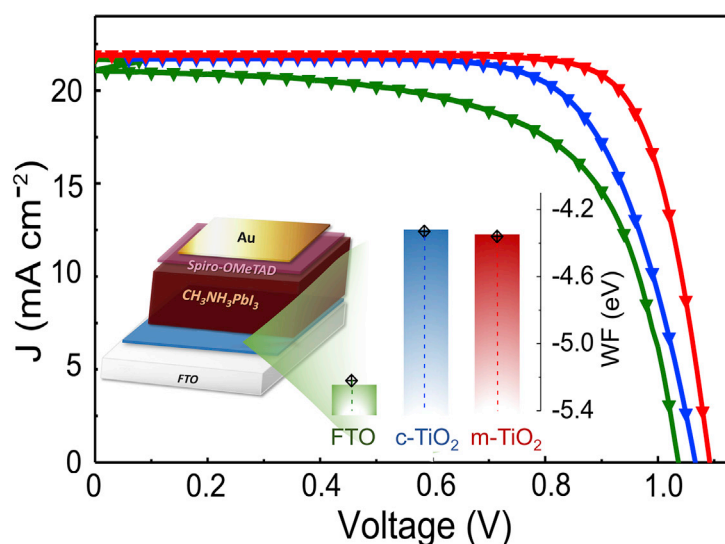


## Article

# Influence of Charge Transport Layers on Open-Circuit Voltage and Hysteresis in Perovskite Solar Cells



Sandheep Ravishankar, Saba Gharibzadeh, Cristina Roldán-Carmona, ..., Nobert Koch, Juan Bisquert, Mohammad Khaja Nazeeruddin

cristina.roldancarmona@epfl.ch (C.R.-C.)  
bisquert@uji.es (J.B.)  
mdkhaja.nazeeruddin@epfl.ch (M.K.N.)

## HIGHLIGHTS

The interplay between the charge-transporting layers and open-circuit potential

The nature of the contacts: a critical factor for the interfacial charge accumulation

The quasi-Fermi level splitting and recombination inside the perovskite rules the  $V_{OC}$

The electric field is not the dominant extraction mechanism for the photocarriers

Perovskite materials are becoming a major player for the future energy scenario. In only a few years, they have demonstrated extraordinary capabilities for optoelectronic applications, promising the highest efficiency at the lowest cost. However, despite the numerous studies reported in the literature, the photophysical behavior and device physics for this new technology remain unclear. Here we reveal fundamental insights into the operation mechanism of the state-of-the-art perovskite solar cells, shedding light on the origins of the open-circuit potential and the hysteretic behavior.

Article

# Influence of Charge Transport Layers on Open-Circuit Voltage and Hysteresis in Perovskite Solar Cells

Sandheep Ravishankar,<sup>1,7</sup> Saba Gharibzadeh,<sup>2,3,7</sup> Cristina Roldán-Carmona,<sup>2,\*</sup> Giulia Grancini,<sup>2</sup> Yonghui Lee,<sup>2</sup> Maryline Ralaifarisoa,<sup>4,5</sup> Abdullah M. Asiri,<sup>6</sup> Nobert Koch,<sup>4,5</sup> Juan Bisquert,<sup>1,\*</sup> and Mohammad Khaja Nazeeruddin<sup>2,8,\*</sup>

## SUMMARY

Perovskite materials have experienced an impressive improvement in photovoltaic performance due to their unique combination of optoelectronic properties. Their remarkable progression, facilitated by the use of different device architectures, compositional engineering, and processing methodologies, contrasts with the lack of understanding of the materials properties and interface phenomena. Here we directly target the interplay between the charge-transporting layers (CTLs) and open-circuit potential ( $V_{OC}$ ) in the operation mechanism of the state-of-the-art  $\text{CH}_3\text{NH}_3\text{PbI}_3$  solar cells. Our results suggest that the  $V_{OC}$  is controlled by the splitting of quasi-Fermi levels and recombination inside the perovskite, rather than being governed by any internal electric field established by the difference in the CTL work functions. In addition, we provide novel insights into the hysteretic origin in perovskite solar cells, identifying the nature of the contacts as a critical factor in defining the charge accumulation at its interface, leading to either ionic, electronic, or mixed ionic-electronic accumulation.

## INTRODUCTION

Despite the impressive improvement in device performance,<sup>1–8</sup> the operating mechanism that governs the high open-circuit potential ( $V_{OC}$ ) and short-circuit current ( $J_{SC}$ ) in perovskite photovoltaics remains unclear. Perovskite solar cells (PSCs) suffer from variations in the current-voltage behavior based on specific experimental parameters, including pre-biasing, light intensity, scan direction, and rate, the set of which have been referred to as dynamic hysteresis.<sup>9</sup> Early studies considered such dynamic hysteresis<sup>10</sup> as the result of a charge collection limitation, conceiving device models in which the transport of charge carriers arises from the built-in electric field, generated through the perovskite layer and modified by the mobile ions.<sup>11,12</sup> Nevertheless, the recent progression in materials processing<sup>13–19</sup> suggests a different scenario, as the state-of-the-art devices possess excellent transport and collection properties, with little to no variation in the photocurrent throughout the scan. In addition, a recent correlation between  $\text{TiO}_2$ /perovskite interface and the output voltage in PSCs<sup>20,21</sup> introduces the question of the role of interfaces in the device operation, calling for deeper investigations of their operation mechanism, with special emphasis on how variations in recombination and/or accumulation at the interfaces affect the hysteretic trends. In this article, we answer some of these questions by investigating the role of the contacts in the transport and recombination of state-of-the-art PSCs. Devices with identical architecture but modified electron-transporting layer (ETL) interface have been examined, using as device configuration

## Context & Scale

Perovskite lead halides are extraordinary low-cost materials and outstanding candidates for an efficient electricity generation. After only a few years of research, perovskite-based technology has been demonstrated to rival those of the prevailing inorganic counterparts, with the advantage of being processed through a variety of easy and cheap fabrication techniques. Nevertheless, such an unprecedented rise in efficiency contrasts with the lack of understanding of the materials properties and interface phenomena, which represents one of the major challenges before its commercialization. Here we provide fundamental insights into the operation mechanism of the state-of-the-art perovskite solar cells, revealing crucial findings on the open-circuit potential  $V_{OC}$  and the hysteretic origin in these cells.

fluorine-doped tin oxide (FTO)/ETL/CH<sub>3</sub>NH<sub>3</sub>PbI<sub>3</sub>/2,2',7,7'-tetrakis-(N,N-di-4-methoxyphenylamino)-9,9'-spirobifluorene (Spiro-OMeTAD)/Au architecture, where different contacts have been carefully chosen: (i) FTO/compact-TiO<sub>2</sub>/mesoporous TiO<sub>2</sub>; (ii) FTO/compact-TiO<sub>2</sub>; and (iii) FTO electrode (ETL-free cell).

## RESULTS

Figure 1A presents a schematic of the cell architecture along with the cross-sectional scanning electron microscopy images in Figure 1B, obtained for each layout. In all cases, the perovskite thickness is ~300 nm, including the mesoporous-based configuration. Interestingly, similar microstructure and layer morphology could be observed for all architectures, independently from the electron-selective contact, as revealed in Figure 1C. In addition, the optical properties of the perovskite films and the X-ray diffraction (XRD) patterns (Figure 1D) were also preserved, showing identical absorption spectra and diffraction patterns corresponding to CH<sub>3</sub>NH<sub>3</sub>PbI<sub>3</sub> tetragonal phase<sup>22</sup> (see also Figure S1). Overall, these results confirm the formation of perovskite films with comparable crystalline quality and optical properties, which is of extreme importance in the upcoming comparative analysis.

The current-voltage (*J*-*V*) curves and the external quantum efficiency (EQE) of the as-prepared solar cells were also analyzed. Figures 2A and 2B show the typical performance of three representative cells corresponding to each device configuration (the characteristic solar cell parameters are reported in Table 1). In agreement with previous works, cells employing a mesoscopic architecture exhibit the best photovoltaic performance (power conversion efficiency [PCE] = 18.75%), followed by the planar cells (PCE = 16.25%) and the ETL-free devices (PCE = 14.03%). Interestingly, *J*<sub>SC</sub> hardly changed with the cell configuration, leading to values over 21 mA·cm<sup>-2</sup> in all cases. These results agree with the EQE spectra exhibited in Figure 2B, which demonstrate a high photon-to-current conversion over 80% for the entire visible spectra, even for the ETL-free device. Nevertheless, the most remarkable value is obtained for the *V*<sub>OC</sub>, remaining close to 1 V in all cases. Such a large *V*<sub>OC</sub> obtained for the ETL-free cells is in contradiction to previous seminal works<sup>15</sup> where a large reduction upon removal of the TiO<sub>2</sub> layer (~0.75 V) was observed and attributed to a reduced built-in potential, generally associated with the non-selectivity of the contact. More recently, a similar behavior was also observed by Juarez-Perez et al. but charge collection was severely reduced, in contrast to our result.<sup>23</sup>

Figures 2C and 2D and Table 1 summarize the photovoltaic performance obtained from more than 40 devices. As deduced from the data, the contact layer is mostly affecting the fill factor (FF) of the cell, which decreases considerably when using a less selective FTO contact, while *J*<sub>SC</sub> and *V*<sub>OC</sub> remain very similar. Comparable results have been also observed for cells containing the mixed cation/mixed halide (FAPbI<sub>3</sub>)<sub>0.85</sub>(MAPbBr<sub>3</sub>)<sub>0.15</sub> perovskite (FA = formamidinium), as illustrated in Figure S2 (see also Table S1). Notably, although slight differences in *J*<sub>SC</sub> and *V*<sub>OC</sub> can be observed for this perovskite composition, a remarkably high *V*<sub>OC</sub> average value over 0.8 V (with a maximum of 0.96 V) is obtained for the ETL-free cell, further generalizing our previous observations.

To verify the electronic structure of the different contact layers, we analyzed them by UV photoelectron spectroscopy (UPS). The results are presented in Figure S3 and the extracted work functions are also illustrated in Figure 2D, in comparison with the *V*<sub>OC</sub>. As expected, the FTO layer has the highest work function (−5.22 eV), followed by the blocking TiO<sub>2</sub> (−4.36 eV) and the mesoporous TiO<sub>2</sub> layer (−4.33 eV). Surprisingly, no apparent relation between the obtained *V*<sub>OC</sub> and the work function of the contact can be deduced. This is also observed when inserting a different ETL material such as compact-SnO<sub>2</sub> layer (work function = −4.93 eV), which also leads to unexpectedly high *V*<sub>OC</sub> values close to 1 V (see Figure S4).

<sup>1</sup>Institute of Advanced Materials (INAM), Universitat Jaume I, 12006 Castelló, Spain

<sup>2</sup>GMF, Institute of Chemical Sciences and Engineering, EPFL Valais, Rue de L'Industrie, 1951 Sion, Switzerland

<sup>3</sup>Department of Physics, Tarbiat Modares University, P.O. Box 14115-175, Tehran, Iran

<sup>4</sup>Humboldt-Universität zu Berlin, Institut für Physik & IRIS Adlershof, Berlin, Germany

<sup>5</sup>Helmholtz-Zentrum Berlin für Materialien und Energie, Division Renewable Energies, Berlin, Germany

<sup>6</sup>Center of Excellence for Advanced Materials Research (CEAMR), King Abdulaziz University, PO Box 80203, Jeddah 21589, Saudi Arabia

<sup>7</sup>These authors contributed equally

<sup>8</sup>Lead Contact

\*Correspondence: [cristina.rolandcarmona@epfl.ch](mailto:cristina.rolandcarmona@epfl.ch) (C.R.-C.), [bisquert@uji.es](mailto:bisquert@uji.es) (J.B.), [mdkhaja.nazeeruddin@epfl.ch](mailto:mdkhaja.nazeeruddin@epfl.ch) (M.K.N.)

<https://doi.org/10.1016/j.joule.2018.02.013>

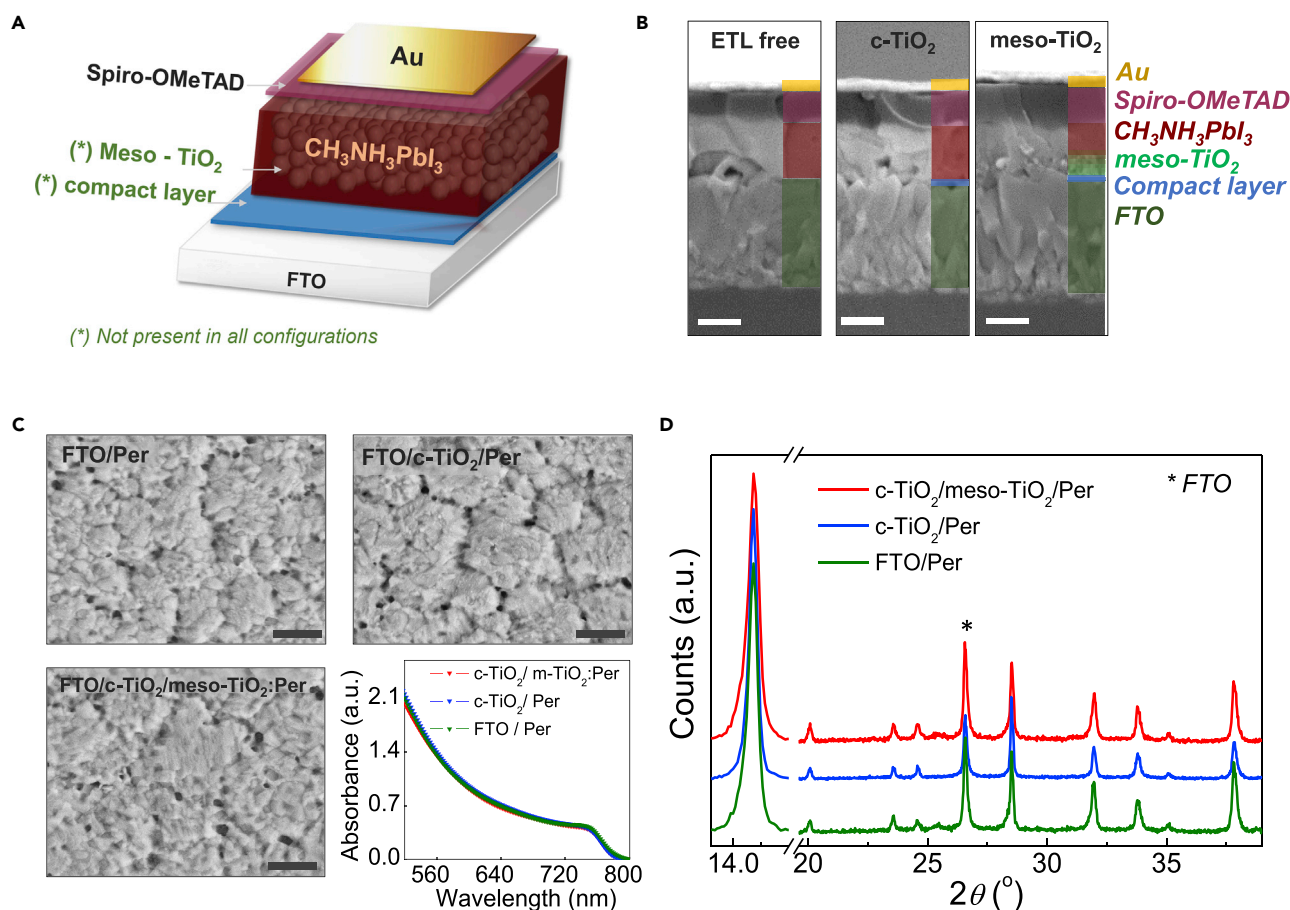


**Figure 1. Solar Cell Configurations, Film Characterization, and Photovoltaic Performance of the Perovskite Cells**

(A) Schematic of the cell architectures. Compact and mesoporous TiO<sub>2</sub> (meso-TiO<sub>2</sub>) layers differ between configurations. (B) Cross-sectional scanning electron microscopy images obtained for each representative layout. Scale bar, 1  $\mu$ m. (C) Surface scanning electron microscopy images and optical properties of perovskite films analyzed in (B). Scale bar, 1  $\mu$ m. (D) XRD patterns of films analyzed in (C).

To obtain insight into the electronic operation of the contacts, we investigated the hysteresis features and capacitive nature of these devices via impedance spectroscopy (IS). Figure 3A shows the *J*-*V* curves obtained for the three systems measured under scan rates ranging from 10 to 200 mV/s. In all cases, the hysteresis loop between forward-reverse (FR) scans “opens up” and scales with the scan rate, as typically occurs in a capacitive discharge superimposed onto the steady-state curve. We note that this effect is maximized in the planar c-TiO<sub>2</sub> cells but minimized for the mesoscopic architecture, suggesting meso-TiO<sub>2</sub> as the main factor responsible for reducing the overall hysteresis, as is often reported in the literature.<sup>24</sup> However, upon removal of the c-TiO<sub>2</sub> layer, the hysteresis is again reduced except for very fast scans, denoting c-TiO<sub>2</sub>/perovskite as the true dominant interface (see Figure S5).<sup>25</sup> Surprisingly, the FTO/perovskite interface also showed strong capacitive trends, indicating a similar mechanism.

## DISCUSSION

According to established photovoltaic knowledge, when a semiconductor light absorber sandwiched between two contacts of very different work function comes to equilibrium, the difference of work functions implies a built-in electrical field that has

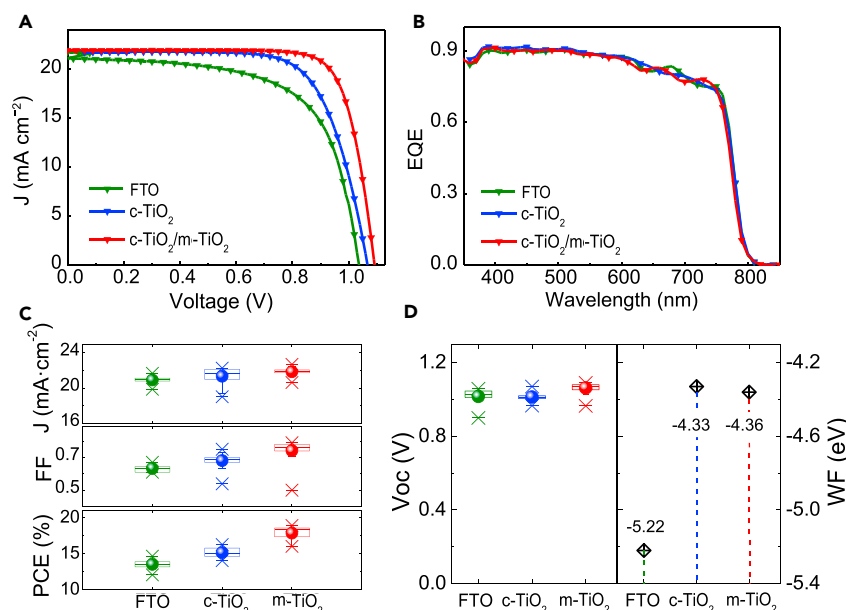


**Figure 2. J-V Performance and Statistical Analysis of Perovskite Solar Cells**

(A and B) Current-voltage (J-V) curves measured under 1 sun illumination (A) and external quantum efficiency (EQE) (B) of representative solar cells containing meso- $\text{TiO}_2$ ,  $c\text{-TiO}_2$ , and ETL-free architectures (for which  $J_{\text{integrated}}$  is  $21.2 \text{ mA cm}^{-2}$ ,  $21.5 \text{ mA cm}^{-2}$ , and  $21.3 \text{ mA cm}^{-2}$ , respectively).

(C and D) Summary of device parameters obtained for more than 40 cells measured under AM 1.5G sun illumination, room temperature, and air conditions (C, left panel in D). The work function of the different contact layers are also indicated for comparison (right panel in D). Legend: (T), maximum value; (L), minimum value; (●), mean value; (□), region containing 25%–75% of the data.

a major role in the transport and extraction of charge. This is usually termed the p-i-n model. On the other hand, 25 years of study of dye-sensitized solar cells and similar devices clearly showed that many solar cells absorb the difference of work functions at the absorber/contact interface, and the electrical field in the device plays a minor role.<sup>26</sup> Here we show that this is a main principle of operation of the PSC, since the  $V_{oc}$  remains stable over a striking modification in the work function of the electron-selective contact, which has the same variation as the  $V_{oc}$  itself, as shown in Figure 2D. Independently of the built-in electric field across the perovskite, the mesoporous morphology, and the difference in work functions across the interfaces, each selective contact will follow the Fermi level of the respective carrier, implying that the main control of open-circuit voltage is established by recombination.<sup>27</sup> This view of the operation mechanism in perovskite devices is also consistent with the results obtained from Kelvin probe force microscopy made on cross-sectional planar  $\text{CH}_3\text{NH}_3\text{PbI}_3$  devices, which show a flat potential distribution in the absorber layer while most of the potential drops are located at selective contact interfaces.<sup>28</sup>

Under cycling conditions of  $10 \text{ mV/s}$ , our systems show high  $V_{oc}$  values for both FR and RF (reverse-forward) scans. This opposes the general assumption that a built-in electric field generated by the difference in the work functions of the two contacts mediates the charge collection. On the contrary, it demonstrates that the built-in electric field is not a major factor governing the extraction of carriers, while carrier transport to contacts is mainly due to diffusion, probably granted by the extremely large diffusion length in these materials. As large charge accumulation combining ionic and electronic charge occurs at the outer interfaces, for state-of-the-art devices hysteretic variations can be directly correlated to the nature of the perovskite crystal

**Table 1. Device Parameters Obtained from the Cell Configurations**

Cell	$J_{SC}$ (mA cm <sup>2</sup> )	$V_{OC}$ (V)	FF	PCE (%)
Meso-TiO <sub>2</sub>	21.91 (21.9 ± 0.8)	1.09 (1.078 ± 0.007)	0.78 (0.77 ± 0.02)	18.75 (18.17 ± 0.8)
c-TiO <sub>2</sub>	21.7 (21.2 ± 0.9)	1.07 (1.02 ± 0.03)	0.70 (0.67 ± 0.05)	16.25 (15 ± 1)
FTO	21.08 (21.1 ± 0.6)	1.04 (0.98 ± 0.08)	0.64 (0.62 ± 0.03)	14.03 (14 ± 1)

The cell configurations are shown in Figure 2. The average values obtained for each device configuration are shown in parentheses.

in contact with the selective layers, which further underlines the importance of understanding the capacitive trends in these devices.

Figure 3B presents the evolution of the capacitance obtained for each device configuration as a function of frequency (in the dark) at different applied voltages. In general, the capacitance shows a stable plateau at high frequency due to dielectric relaxation in the bulk, and low-frequency large values that grow further with the applied voltage, directly probing the contact properties. Importantly, the low-frequency value increases more than two orders of magnitude from 10 μF at low frequencies (~100 mHz) to a maximum capacitance of 10 mF for ~1 V. We interpret this capacitance as an accumulation layer of ionic (cations) and electronic carriers (holes) at the c-TiO<sub>2</sub> contact with the perovskite.<sup>29</sup> The capacitance for ion accumulation is described by the Guoy-Chapman model, whose voltage-dependence for voltages above  $k_B T/q$  is given by

$$C = \left( \frac{z^2 q^2 n_i^0 \epsilon_r \epsilon_0}{2k_B T} \right)^{1/2} \cdot \exp\left(\frac{zqV}{m_C k_B T}\right), \quad (\text{Equation 1})$$

where  $z$  is the charge number of the ions,  $q$  the electronic charge,  $n_i^0$  the ionic concentration in the bulk, and  $\epsilon_r$  and  $\epsilon_0$  the relative and vacuum dielectric constants, respectively.  $m_C$  is a capacitive exponent with the value 2. However, a similar equation is also used for the accumulation of majority carriers at the interface,<sup>30</sup> again with  $m_C = 2$ , hindering the distinction between ionic and electronic accumulation through only capacitance measurements. In our case, there is a difference in the way the low-frequency capacitance changes with voltage between the different electron-contacts samples. The cells containing meso-TiO<sub>2</sub> exhibit a sharp increase after 0.6 V. Planar c-TiO<sub>2</sub> cells show a similar evolution, although a negative capacitance region is perceived, whose onset is characterized by the downward spike, located around 100 Hz. The negative capacitance, well documented in the literature, is interpreted as the accumulation and subsequent discharge of both ionic and electronic carriers (holes) at the TiO<sub>2</sub>/perovskite interface.<sup>31</sup> Finally, ETL-free samples do not show the negative capacitance trend, but a continuous and exponential evolution of the low-frequency capacitance with voltage, noted in Figure 3C. We can therefore conclude that low-frequency capacitance at low and very high voltage shows similar trends in the three different PSCs, but the intermediate voltages and the larger frequency region variations indicate dynamic modifications in charge accumulation (ionic/electronic) that have significant consequences on the nature and timescales in a transient experiment, altering the hysteretic trends considerably. This observation correlates well with the different dynamic hysteresis responses observed previously.

To investigate the processes at the perovskite/ETL interface, we performed a dynamical optical investigation by means of transient absorption spectroscopy (TAS) in the nanosecond domain, as depicted in Figure 4. We monitored the TAS spectral



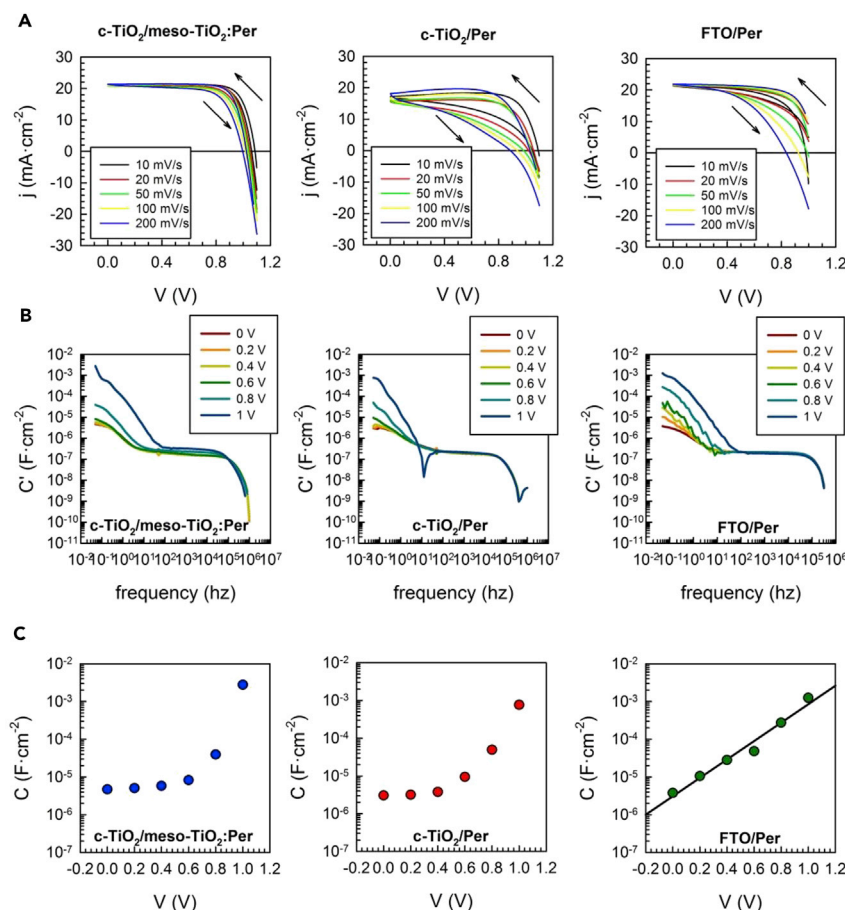


**Figure 3. Hysteresis Behavior and Impedance Spectroscopy Analysis**

(A) J-V scans for perovskite cells containing the three investigated ETL contacts (scan rates indicated in the legend).

(B) Absolute real values of the capacitance obtained from electrochemical impedance spectroscopy measurements in the dark.

(C) Evolution of the low-frequency capacitance versus applied voltage for the three investigated cells. The linear fit of  $\ln C$  versus voltage for the ETL-free cell shows a slope of 5.62.

evolution of the three different samples upon excitation with a light pulse at 600 nm, ensuring a light penetration depth of less than 200 nm.<sup>32</sup> Note that we keep the excitation density constant on the three samples, which have the same thickness, ensuring that a similar carrier density is generated. As reported in Figures 4A–4C, a negative band peaking at 760 nm appears, which is assigned to photobleaching (PB), due to state filling of the conduction and valence band. Notably, the PB signal is proportional to the density of charges and its dynamical evolution reflects the charge dynamics. The PB band decreases in the time range investigated, as shown by the normalized dynamic at the 760-nm probe wavelength presented in Figure 4D. It reveals a fast decay with a time constant of  $t = 100$  ns, accompanied by a longer component that does not decay in our temporal window (1.5  $\mu$ s) (a comparison of the decay in the 100-ns range is reported in the inset of Figure 4B). Since we use an excitation density of around 50 nJ/cm<sup>2</sup> corresponding to a charge density of around  $10^{17}$  cm<sup>-3</sup>, most of the traps are expected to be filled, thus the PB decay mainly mirrors the electron hole recombination. However, the PB signal persists on a longer timescale. As already observed by Leijtens et al., the long-living component appearing in the TAS as well as in transient photocurrent measurements can be related to

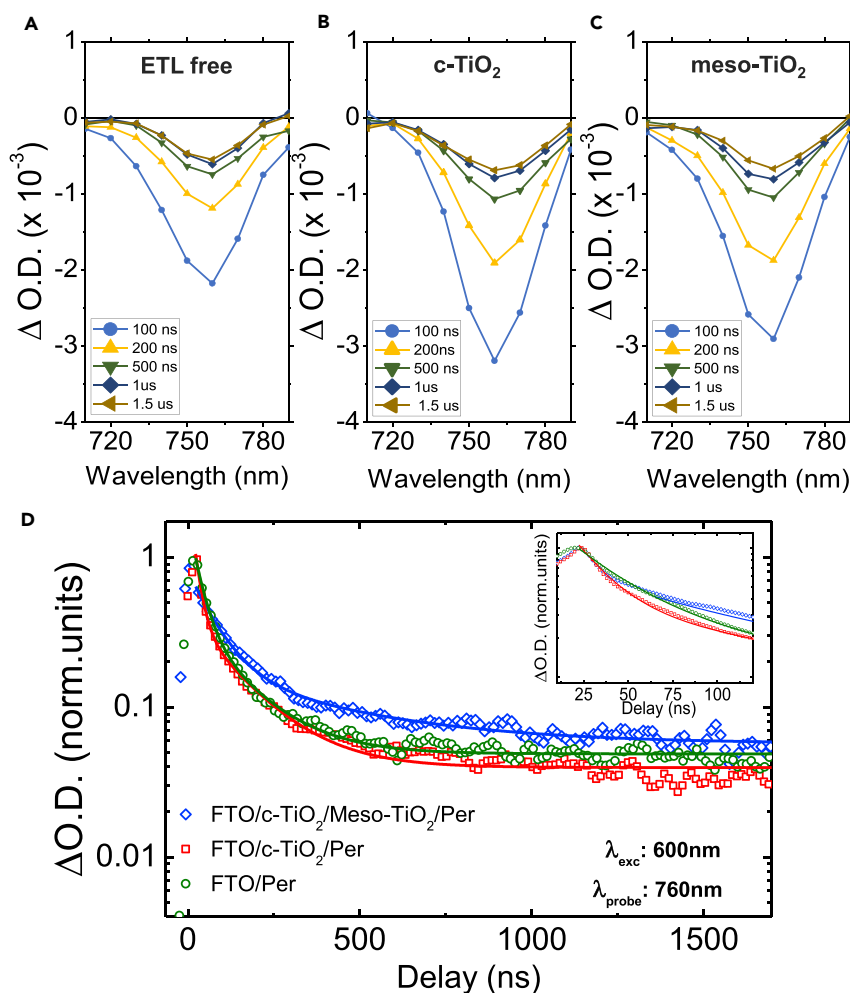


**Figure 4. Dynamical Optical Investigation Using Transient Absorption Spectroscopy**

(A–C) TAS spectral evolution at the FTO/perovskite interface (A), c-TiO<sub>2</sub>/perovskite interface (B), and meso-TiO<sub>2</sub>/perovskite interface (C) measured upon excitation from the glass side with an incident light pulse at 600 nm (penetration depth  $\sim 200$  nm).<sup>25</sup>  
(D) Dynamics at 760 nm revealing a faster time constant of  $t = 100$  ns.

trap-mediated recombination, i.e., trapped electrons or holes.<sup>33</sup> Considering the same optical density for the three films and the same excitation density used, we can infer from the initial spectra (at 0- to 200-ns time window) that the photoinduced charge density at the compact-TiO<sub>2</sub>/perovskite interface is slightly higher. However, for all cases the long-living component, sometimes also visible in photoluminescence measurements and still debated, can be related to the presence of long-living accumulated charges (possibly holes),<sup>34</sup> located at the perovskite/ETL surface. Interestingly, the signal evolution (i.e., time constant) and magnitude of the long-living component is similar in all cases, providing a clear indication that the interface charge dynamics in the nanosecond-microsecond timescale, relevant for the photovoltaic action in terms of charge collection, do not considerably differ when comparing meso-TiO<sub>2</sub>, c-TiO<sub>2</sub>, or FTO interfaces. On the other hand, on the shorter timescale, the PB of the meso-TiO<sub>2</sub> interface decays more slowly (a time constant of 50 ns is retrieved from fitting, as shown in Table 2), which might reflect a reduced electron hole recombination possibly due to reduced charge accumulation at this interface. This observation is in agreement with the slightly higher  $V_{OC}$  that this sample presents



**Table 2. Optical Analysis**

Sample	$t_1$ (ns)	$t_2$ (ns)
FTO/MAPbI <sub>3</sub>	21	98
FTO/c-TiO <sub>2</sub> /MAPbI <sub>3</sub>	13	98
FTO/c-TiO <sub>2</sub> /MesoTiO <sub>2</sub> /MAPbI <sub>3</sub>	50	269

Optical parameters obtained from the TAS analysis.

over the others. A direct link with the device behavior is rather challenging; however, the reduced charge accumulation at the meso-TiO<sub>2</sub> interface might be a possible reason, among others, for the minimized dynamic hysteresis response for the mesoporous-based solar cell. Further work is ongoing to elucidate the interface dynamics and better establish a connection to the device scale.

We can therefore conclude that, while it is widely believed that the role of selective contacts toward photovoltage operates by controlling the built-in voltage, here we demonstrate that it rather depends on the internal recombination and splitting of Fermi levels inside the perovskite material. Our results indicate that the electric field is not the dominant charge extraction mechanism for the photocarriers, and very different electron contacts based on the metal oxide/perovskite interface can behave similarly. Furthermore, the nature of the contact can drastically influence the dynamic response of charge accumulation at the interface, being an essential actor in controlling hysteresis and pre-treatment dependence in time-transient experiments.

## EXPERIMENTAL PROCEDURES

### Solar Cell Fabrication

PSCs were fabricated on F-doped SnO<sub>2</sub> (NSG10) substrates previously cleaned by a sequential sonication treatment in a 2% Hellmanex solution, acetone, and isopropanol, followed by UV ozone treatment for 15 min. These substrates were directly used as described for the ETL-free PSCs. To prepare the other configurations investigated in this article, we deposited a compact blocking layer of TiO<sub>2</sub> (c-TiO<sub>2</sub>, 30 nm in thickness) by spray pyrolysis using a titanium diisopropoxide bis(acetylacetonate) solution in ethanol (22% v/v), followed by sintering at 450°C for 20 min (c-TiO<sub>2</sub> electrode). SnO<sub>2</sub> electrodes were prepared by spin-coating a precursor solution of SnCl<sub>4</sub> (Acros) dissolved in water. For formation of a ~100-nm thick SnO<sub>2</sub> layer, 0.5 M SnCl<sub>4</sub> solution was spin-coated on the UV-ozone-treated FTO substrates at 5,000 rpm for 10 s. The SnO<sub>2</sub> film was then transferred onto a hotplate and dried at 100°C for 1 min, post-annealed at 180°C for 1 hr, and cooled down before deposition of perovskite. The planar configurations, including the ETL-free cells, were treated by UV ozone for 15 min before deposition of the perovskite layer. Finally, a 150-nm thick layer of mesoporous TiO<sub>2</sub> (meso-TiO<sub>2</sub>, 30 NR-D titania paste from Dyesol) was prepared by spin-coating a diluted TiO<sub>2</sub> dispersion in ethanol (150 mg·mL<sup>-1</sup>) at 2,000 rpm for 15 s followed by a sintering step at 450°C for 30 min. Afterward, the meso-TiO<sub>2</sub> substrates were lithium-treated by spin-coating 40 μL of tris(bis(trifluoromethylsulfonyl)imide) (Li-TFSI, 10 mg/mL in acetonitrile) onto the mesoporous layer, followed by an additional sintering step at 450°C for 20 min. After sintering, the c-TiO<sub>2</sub>/meso-TiO<sub>2</sub> electrodes were ready to use and transferred to an N<sub>2</sub> controlled atmosphere. The perovskite precursor solution was prepared by mixing CH<sub>3</sub>NH<sub>3</sub>I (MAI, Dyesol) and PbI<sub>2</sub> (TCl) in N,N'-dimethylsulfoxide (DMSO) in a molarity of 1.20 for MAPbI<sub>3</sub>, while for the mixed cation/halide composition formamidinium iodide (FAI), MAI (from Dyesol), PbI<sub>2</sub>, and PbBr<sub>2</sub> (TCl) were mixed in DMF/DMSO (4:1) solvent at 1.25 M to form (FAPbI<sub>3</sub>)<sub>0.85</sub>(MAPbBr<sub>3</sub>)<sub>0.15</sub>, with 5% of PbI<sub>2</sub> excess content. The perovskite layers were then fabricated by using

a two-step spin-coating process reported by Seok et al.<sup>11</sup> (first step 1,000 rpm for 10 s; second step 4,000 rpm for 30 s), and 10 s prior to the end of the program 100  $\mu$ L of chlorobenzene was poured onto the films. The substrates were then annealed at 100°C for 60 min. Afterward, Spiro-OMeTAD was spin-coated at 4,000 rpm from a chlorobenzene solution (28.9 mg in 400  $\mu$ L, 60 mmol) containing Li-TFSI (7.0  $\mu$ L from a 520 mg/mL stock solution in acetonitrile), TBP (11.5  $\mu$ L), and Co(II)TFSI (10 mol%, 8.8  $\mu$ L from a 40 mg/mL stock solution) as dopants. Finally, a 70 nm gold electrode was evaporated.

### Thin Film Characterization

The XRD patterns of the prepared films were measured using a D8 Advance diffractometer from Bruker (Bragg-Brentano geometry, with an X-ray tube Cu-K $\alpha$ ,  $\lambda$  = 1.5406 Å). The absorption spectra were registered with a UV-Vis-IR spectrophotometer (PerkinElmer). Photoelectron spectroscopy (PES) measurements were performed in an ultra-high vacuum analysis chamber (base pressure of  $2 \times 10^{-10}$  mbar) using an He-discharge UV source (Omicron) with an excitation energy of 21.2 eV for UPS. Before the analysis, the samples were treated by UV ozone for 15 min in the same conditions as for the device preparation. The photoelectron spectra were recorded using a Phoibos 100 (Specs) hemispherical energy analyzer at a pass energy of 5 eV for the valence band. For work function determination, the secondary electron cutoff (SECO) was recorded by applying a –10 V sample bias to clear the analyzer work function. The reported valence band spectra were background subtracted. The binding energies for all the photoemission spectra are referenced to the Fermi level. For the nanosecond-TAS/photoluminescence a nanosecond laser (5 ns pulse duration, 10 Hz, Ekspla NT342 model) with an integrated optical parametric oscillator system (from 355 to 2,500 nm tunability) was used as pump source. This was coupled with the LP980-KS Laser Flash Photolysis Spectrometer used for the measurement of laser-induced transient absorption and the photoluminescence kinetics and spectra. Wavelength-specific kinetic measurements were made using a photomultiplier and a digital storage oscilloscope. The probe light was provided by a pulsed xenon arc lamp. The beams were focused onto the sample on a minimum 5-mm<sup>2</sup> diameter area, ensuring the spatial overlap. The transmitted probe was spectrally filtered by a monochromator and detected. From the transmission change following photoexcitation, the variation in the absorption was thus derived as  $\Delta O(\tau, \lambda) = \log(I_{\text{probe}}/I_t(\tau, \lambda))$ , where  $I_{\text{probe}}$  is the transmitted probe with excitation off and  $I_t$  is the transmitted probe after laser excitation. The minimum detectable optical density of the LP980-KS using the photomultiplier is  $\Delta OD = 0.002$  (single-shot, fast-detector option) with a system overall response function of: <7 ns (laser limited).

### Device Characterization

The photovoltaic device performance was analyzed using a VeraSol LED solar simulator (Newport) producing 1 sun AM 1.5 (1,000 W/m<sup>2</sup>) sunlight. Current-voltage curves were measured in air with a potentiostat (Keithley 2604). The light intensity was calibrated with an NREL-certified KG5 filtered Si reference diode. The solar cells were masked with a metal aperture of 0.16 cm<sup>2</sup> to define the active area. Current-voltage curves at different scan rates were collected from slowest to fastest scan rate by scanning in the FR direction followed by the RF direction for a given scan rate, with a time interval of 10 s (under illumination) before the next measurement. The starting voltage for the FR scan was slightly higher (30 mV) than the  $V_{OC}$  of the device while for the RF scan, it was 0 V. EQE was measured with the IQE200B (Oriel) without bias light. IS measurements were performed in the dark for a cell area of 0.56 cm<sup>2</sup>. A perturbation amplitude of 10 mV was used and the spectra measured over the frequency range 50 mHz to 1 MHz.

## SUPPLEMENTAL INFORMATION

Supplemental Information includes five figures and one table and can be found with this article online at <https://doi.org/10.1016/j.joule.2018.02.013>.

## ACKNOWLEDGMENTS

S.R. acknowledges Generalitat Valenciana for the grant GRISOLIA/2014/034. J.B. acknowledges funding from MINECO of Spain under Project MAT2016-76892-C3-1-R and Generalitat Valenciana Project PROMETEOII/2014/020. G.G. acknowledges the Swiss National Science Foundation (SNSF) funding through the Ambizione Energy project HYPER (grant number PZENP2\_173641). M.K.N. acknowledges financial support from European Commission H2020-ICT-2014-1, SOLEDLIGHT project, grant agreement N1: 643791, the Swiss State Secretariat for Education, Research and Innovation (SERI), and CTI 15864.2 PFNM-NM, Solaronix, Aubonne, Switzerland. N.K. and M.R. were supported by the SFB951 (DFG).

## AUTHOR CONTRIBUTIONS

S.G. and C.R.-C. fabricated the devices and carried out the majority of measurements. S.R. performed the impedance analysis. G.G. carried out the spectroscopic analysis. Y.L. prepared the SnO<sub>2</sub> electrodes and mixed cation perovskite layers. M.R. and N.K. performed the UPS characterization. C.R.-C., J.B., and M.K.N. wrote the manuscript and interpreted the data. A.M.A. assisted in data analysis. M.K.N. directed and supervised the project leading to this publication.

## DECLARATION OF INTERESTS

The authors declare no competing interests.

Received: September 16, 2017

Revised: January 19, 2018

Accepted: February 14, 2018

Published: March 12, 2018

## REFERENCES

- Shin, S.S., Yeom, E.J., Yang, W.S., Hur, S., Kim, M.G., Im, J., Seo, J., Noh, J.H., and Seok, S.I. (2017). Colloidally prepared La-doped BaSnO<sub>3</sub> electrodes for efficient, photostable perovskite solar cells. *Science* 356, 167–171.
- Xiao, Z., Kerner, R.A., Zhao, L., Tran, N.L., Lee, K.M., Koh, T.-W., Scholes, G.D., and Ran, B.P. (2017). Efficient perovskite light-emitting diodes featuring nanometre-sized crystallites. *Nat. Photon.* 11, 108–115.
- Fang, Y., Dong, Q., Shao, Y., Yuan, Y., and Huang, J. (2015). Highly narrowband perovskite single-crystal photodetectors enabled by surface-charge recombination. *Nat. Photonics* 9, 679–686.
- Senanayak, S.P., Yang, B., Thomas, T.H., Giesbrecht, N., Huang, W., Gann, E., Nair, B., Goedel, K., Guha, S., Moya, X., et al. (2017). Understanding charge transport in lead iodide perovskite thin-film field-effect transistors. *Sci. Adv.* 3, e1601935.
- Xu, J., Chen, Y., and Dai, L. (2015). Efficiently photo-charging lithium-ion battery by perovskite solar cell. *Nat. Commun.* 6, 8103.
- Xing, G., Mathews, N., Sun, S., Lim, S.S., Lam, Y.M., Grätzel, M., Mhaisalkar, S., and Sum, T.C. (2013). Long-range balanced electron- and hole-transport lengths in organic-inorganic CH<sub>3</sub>NH<sub>3</sub>PbI<sub>3</sub>. *Science* 342, 344–347.
- Zhu, H., Fu, Y., Meng, F., Wu, X., Gong, Z., Ding, Q., Gustafsson, M.V., Trinh, M.T., Jin, S., and Zhu, X.Y. (2015). Lead halide perovskite nanowire lasers with low lasing thresholds and high quality factors. *Nat. Mater.* 14, 636–642.
- Kagan, C.R., Mitzi, D.B., and Dimitrakopoulos, C.D. (1999). Organic-inorganic hybrid materials as semiconducting channels in thin-film field-effect transistors. *Science* 286, 945–947.
- Ravishankar, S., Almora, O., Echeverría-Arrondo, C., Ghahremanirad, E., Aranda, C., Guerrero, A., Fabregat-Santiago, F., Zaban, A., Garcia-Belmonte, G., and Bisquert, J. (2017). Surface polarization model for the dynamic hysteresis of perovskite solar cells. *J. Phys. Chem. Lett.* 8, 915–921.
- Shen, H., Jacobs, D.A., Wu, Y., Duong, T., Peng, J., Wen, X., Fu, X., Karuturi, S.K., White, T.P., Weber, K., et al. (2017). Inverted hysteresis in CH<sub>3</sub>NH<sub>3</sub>PbI<sub>3</sub> solar cells: role of stoichiometry and band alignment. *J. Phys. Chem. Lett.* 8, 2672–2680.
- Tress, W., Marinova, N., Moehl, T., Zakeeruddin, S.M., Nazeeruddin, M.K., and Grätzel, M. (2015). Understanding the rate-dependent J-V hysteresis, slow time component, and aging in CH<sub>3</sub>NH<sub>3</sub>PbI<sub>3</sub> perovskite solar cells: the role of a compensated electric field. *Energy Environ. Sci.* 8, 995–1004.
- Richardson, G., O’Kane, S.E.J., Niemann, R.G., Peltola, T.A., Foster, J.M., Cameron, P.J., and Walker, A.B. (2016). Can slow-moving ions explain hysteresis in the current-voltage curves of perovskite solar cells? *Energy Environ. Sci.* 9, 1476–1485.
- Burschka, J., Pellet, N., Moon, S.J., Humphry-Baker, R., Gao, P., Nazeeruddin, M.K., and Grätzel, M. (2013). Sequential deposition as a route to high-performance perovskite-sensitized solar cells. *Nature* 499, 316–319.
- Malinkiewicz, O., Yella, A., Lee, Y.H., Espallargas, G.M., Graetzel, M., Nazeeruddin,

- M.K., and Bolink, H.J. (2014). Perovskite solar cells employing organic charge-transport layers. *Nat. Photon.* **8**, 128–132.
15. Jeon, N.J., Noh, J.H., Yang, W.S., Kim, Y.C., Ryu, S., Seo, J., and Seok, S.I. (2015). Compositional engineering of perovskite materials for high-performance solar cells. *Nature* **517**, 476–480.
16. Park, N.G. (2016). Methodologies for high efficiency perovskite solar cells. *Nano Converg.* **3**, 15.
17. Lim, K.G., Kim, H.B., Jeong, J., Kim, H., Kim, J.Y., and Lee, T.W. (2014). Boosting the power conversion efficiency of perovskite solar cells using self-organized polymeric hole extraction layers with high work function. *Adv. Mater.* **26**, 6461–6466.
18. Lim, K.G., et al. (2016). Self-doped conducting polymer as a hole-extraction layer in organic-inorganic hybrid perovskite solar cells. *Adv. Mater. Interfaces* **3**, <https://doi.org/10.1002/admi.201500678>.
19. Lim, K.-G., Ahn, S., Kim, Y.-H., Qi, Y., and Lee, T.-W. (2016). Universal energy level tailoring of self-organized hole extraction layers in organic solar cells and organic-inorganic hybrid perovskite solar cells. *Energy Environ. Sci.* **9**, 932–939.
20. Gottesman, R., Lopez-Varo, P., Gouda, L., Jimenez-Tejada, J.A., Hu, J., Tirosh, S., Zaban, A., and Bisquert, J. (2016). Dynamic phenomena at perovskite/electron-selective contact interface as interpreted from photovoltage decays. *Chem* **1**, 776–789.
21. Rong, Y., Hu, Y., Ravishankar, S., Liu, H., Hou, X., Sheng, Y., Mei, A., Wang, Q., Li, D., Xu, M., et al. (2017). Tunable hysteresis effect for perovskite solar cells. *Energy Environ. Sci.* **10**, 2383–2391.
22. Rong, Y., Tang, Z., Zhao, Y., Zhong, X., Venkatesan, S., Graham, H., Patton, M., Jing, Y., Guloy, A.M., and Yao, Y. (2015). Solvent engineering towards controlled grain growth in perovskite planar heterojunction solar cells. *Nanoscale* **7**, 10595–10599.
23. Juarez-Perez, E.J., Wußler, M., Fabregat-Santiago, F., Lakus-Wollny, K., Mankel, E., Mayer, T., Jaegermann, W., and Mora-Sero, I. (2014). Role of the selective contacts in the performance of lead halide perovskite solar cells. *J. Phys. Chem. Lett.* **5**, 680–685.
24. Kim, H.-S., and Park, N.-G. (2014). Parameters affecting I-V hysteresis of  $\text{CH}_3\text{NH}_3\text{PbI}_3$  perovskite solar cells: effects of Perovskite crystal size and mesoporous  $\text{TiO}_2$  layer. *J. Phys. Chem. Lett.* **5**, 2927–2934.
25. Sanchez, R.S., Gonzalez-Pedro, V., Lee, J.W., Park, N.G., Kang, Y.S., Mora-Sero, I., and Bisquert, J. (2014). Slow dynamic processes in lead halide perovskite solar cells. Characteristic times and hysteresis. *J. Phys. Chem. Lett.* **5**, 2357–2363.
26. Bisquert, J. (2017). *The Physics of Solar Cells: Perovskites, Organics, and Photovoltaic Fundamentals* (CRC Press).
27. Würfel, U., Cuevas, A., and Wuerfel, P. (2015). Charge carrier separation in solar cells. *IEEE J. Photovolt.* **5**, 461–469.
28. Bergmann, V.W., Guo, Y., Tanaka, H., Hermes, I.M., Li, D., Klasen, A., Bretschneider, S.A., Nakamura, E., Berger, R., and Weber, S.A. (2016). Local time-dependent charging in a perovskite solar cell. *ACS Appl. Mater. Interfaces* **8**, 19402–19409.
29. Garcia-Belmonte, G., and Bisquert, J. (2016). Distinction between capacitive and noncapacitive hysteretic currents in operation and degradation of perovskite solar cells. *ACS Energy Lett.* **1**, 683–688.
30. Zarazua, I., Bisquert, J., and Garcia-Belmonte, G. (2016). Light-induced space-charge accumulation zone as photovoltaic mechanism in perovskite solar cells. *J. Phys. Chem. Lett.* **7**, 525–528.
31. Ghahremanirad, E., Bou, A., Olyae, S., and Bisquert, J. (2017). Inductive loop in the impedance response of perovskite solar cells explained by surface polarization model. *J. Phys. Chem. Lett.* **8**, 1402–1406.
32. Berera, R., van Grondelle, R., and Kennis, J.T. (2009). Ultrafast transient absorption spectroscopy: principles and application to photosynthetic systems. *Photosynth. Res.* **101**, 105–118.
33. Leijtens, T., Eperon, G.E., Barker, A.J., Grancini, G., Zhang, W., Ball, J.M., Kandada, A.R.S., Snaith, H.J., and Petrozza, A. (2016). Carrier trapping and recombination: the role of defect physics in enhancing the open circuit voltage of metal halide perovskite solar cells. *Energy Environ. Sci.* **9**, 3472–3481.
34. Li, W., Liu, J., Bai, F.-Q., Zhang, H.-X., and Prezhdo, O.V. (2017). Hole trapping by iodine interstitial defects decreases free carrier losses in perovskite solar cells: a time-domain ab initio study. *ACS Energy Lett.* **2**, 1270–1278.